SI Appendix

Noise-driven growth rate gain in clonal cellular populations

Mikihiro Hashimoto, Takashi Nozoe, Hidenori Nakaoka, Reiko Okura, Sayo Akiyoshi, Kunihiko Kaneko, Edo Kussell, Yuichi Wakamoto

MATERIALS AND METHODS

Cell strains

We used W3110 and B/r derivative *E. coli* strains in this study. To remove their motility, we knocked out *fliC* from W3110, which encodes flagellin (*fliC* gene does not exist in B/r). We also removed *fimA* and *flu* from both strains to diminish non-specific adhesion to the internal surface of the device and the tubes [1]. We designated those mutated strains constructed from W3110 and B/r as F3 and BrF2, respectively.

To facilitate the image analysis, we introduced fluorescent reporters into F3 and BrF2. F3 rpsL-gfp and BrF2 rpsL-gfp harbor a low copy plasmid, pUA66-rpsL [2, 3], from which GFPmut2 is expressed under the control of the rpsL promoter. F3 T7-venus expresses YFP-Venus [6](40) under the control of T7 promoter integrated at the *intC* locus on the chromosome. We also integrated *lacUV5* promoter and T7 RNA polymerase gene at the *lacZ* locus of the chromosome. *lacUV5* promoter and T7 RNA polymerase gene were cloned from BL21 (DE3) (TAKARA). F3 LVS expresses Venus-SmR fusion protein under the control of *PLlacO-1* promoter [4] from the *intC* locus on the chromosome. F3 LVS was originally constructed for a different study, and employed here as a representative strain that expresses a fluorescent reporter from the chromosome. The streptomycin-resistant gene, smR, was cloned from the plasmid pKP2375 (a kind gift from Dr. Hironori Niki at National Institute of Genetics, Japan).

To create these strains, the genes and the promoters were first assembled on the plasmids. Genome integration and gene knock-out were done according to the standard λ-Red recombination [5]. The names and genotypes of the constructed *E. coli* strains were listed in SI Appendix Table S2.

Culture conditions

We used M9 minimal medium (M9 minimal salt (Difco) + 2 mM $MgSO_4$ (Wako) + 0.1 mM $CaCl_2$ (Wako)) as a base, and supplemented it with either glucose (Wako) + 1/2 MEM amino acids solution (Sigma), glycerol (Wako), casamino acids (Wako) + glucose, or LB medium + 1/2 MEM amino acids solution. The names of the culture media and their compositions are listed in SI Appendix Table S3. For the cultures of F3 T7-venus and F3 LVS, we also added 0.1 mM Isopropyl β-D-1-thiogalactopyranoside (IPTG) as an inducer of the fluorescence reporter. We used two temperature settings, 30°C and 37°C, to prepare different growth conditions.

Microfabrication

For constructing growth channels and flow channels, we prepared two types of photomasks: one for flow channels, and the other for growth channels. For making photomasks, we first coated 1,000-angstrom-thick chromium layer on a clean glass slide by evaporative deposition (SVC-700TM, Sanyu). We then spin-coated a positive photoresist (OFPR-800, Tokyo Ohka Kogyo) on the Cr-coated glass slide. According to the CAD design, we exposed a part of the photoresist layer by laser drawing (DDB-3TH, Neoark), and developed it in NMD-3 (Tokyo Ohka Kogyo). The uncovered part of the Cr-layer was removed in MPM-E30 (INTEC). The remaining photoresist layer was removed by aceton. Lastly, the slide was rinsed in MilliQ water and air-dried.

We implemented two-step chemical etching for fabricating the two types of microchannels on a glass coverslip. First, we coated 1,000-angstrom Cr-layer on a clean coverslip (NEO Micro glass, No. 1., 24 mm×60 mm, Matsunami) by evaporative deposition. We then spin-coated OFPR-800 photoresist and exposed it to UV light utilizing mercury lamp of microscope (Type USH-102D, USHIO) with the photomask for flow channels. After the development of photoresist in NMD-3 and the Cr-patterning in MPM-E30, the exposed part of the coverslip was etched in buffered hydrofluoric acid solution (110-BHF, Morita Kagaku Kogyo) for four hours at 23°C. The etching

reaction was stopped by soaking the coverslip in milliQ water. The remaining photoresist and the Cr-layer were removed by aceton and MPM-E30, respectively. This coverslip was washed by sonication in ethanol and milliQ water for the second round of the channel fabrication. We repeated the same procedure as above for creating growth channels on the coverslip with flow channels except 1) the photomask for growth channels was used; and 2) the duration of chemical etching was 15 min. The final dimension of one flow channel was 2,000 μm (L)×50 μm (W)×15 μm (D), and that of one growth channel was 30 μm (L)×3 μm (W)×1 μm (D) (SI Appendix Fig. S1).

To make PDMS pad with bubble trap groove, we cut out two pieces of 9 mm×1 mm and one piece of 7 mm×1 mm rectangles from frame-seal chamber (Biorad). These were sealed on the bottom of a plastic culture dish to form 9 mm×9 mm ⊓-shape, and used as the mold for PDMS. A well-mixed PDMS (Sylgard 184, Part A: Part B = 10:1) was poured onto the mold with the final target thickness ca. 5 mm. The air bubbles were removed under a decreased pressure for 30 min. The PDMS was cured at 65°C for one hour, and 20 mm×20 mm squared PDMS pad was cut out by blade. We punched out three holes (ϕ =2 mm) at the positions shown in SI Appendix Fig. S1A, and 10-cm long silicone tubes (SR-1554, Tigers Polymer Corp., outer $\phi = 2$ mm, inner $\phi = 1$ mm) were inserted into the holes. The tubes were fixed to the holes by gluing them with a small amount of PDMS. This PDMS pad was washed in isopropanol by sonication and autoclaved for the single-cell measurements.

Chemical decoration of coverslip and cellulose membrane

We first washed the microfabricated coverslip by sonication in contaminon (Wako), ethanol (Wako), and 0.1M NaOH solution (Wako), and dried it at 140°C for 30 min. To create amino group on the glass surface, the washed coverslip was soaked in
1% (v/v) 3-(2-aminoethylaminopropyl)trimethoxysilane solution (Shinetsu Kagaku Kogyo) for 30 min and heated at 140°C for 30 min. The treated coverslip was washed in milliQ water for 15 min, and dried at 140°C for 30 min. 1 mg NHS-LC-LC-Biotin (Funakoshi) was dissolved in 25 μl dimethyl sulfoxide and dispersed in 1 ml phosphate buffer (0.1 mM, pH8.0). 200 μl of this biotin solution was placed on the coverslip, and incubated at room temperature for four hours. The biotin solution was removed by soaking the coverslip in milliQ water.

We used streptavidin-decorated cellulose membrane to cover the growth and flow channels in the device. A 3 cm×3 cm cut cellulose membrane (Spectra/Por 7, MWCO 25,000) was washed in milliQ water, and incubated by gentle shake for four hours at 25°C. After the wash in milliQ water, the treated membrane was incubated in 500-μl solution of streptavidin hydrazyde (Funakoshi) (10 μg/ml, dissolved in 0.1 mM phosphate buffer (pH7.0)) by gentle shake for 14 hours at 25°C. The membrane was again washed in milliQ water and stored at 4°C.

Single-cell time-lapse observation

To prepare *E. coli* cells for single-cell observation, we first inoculated a glycerol stock into 2-ml culture medium, and incubated it by shaking overnight under the same conditions of culture medium and temperature as those used in the time-lapse measurement. 10 μl of the overnight culture was inoculated in 2-ml fresh culture medium and incubated with shaking until the optical density reaches 0.2∼0.5 at λ= 600 nm. This exponential-phase culture was diluted to OD_{600}=0.05, and loaded onto the device.

0.5 μl of the prepared cell culture was spotted on the growth channel region on the coverslip, and covered by the streptavidin-decorated cellulose membrane. Removing an excess cell culture by filter paper allowed the membrane to contact with the glass surface, where the biotin-streptavidin bonding was formed. During this process, a small number of cells were trapped randomly in the growth channels. A 20-μl fresh medium was placed on the membrane to avoid drying, and a PDMS pad was attached to the coverslip via a two-sided-seal frame-seal chamber (Biorad). This device assembly was connected to the silicone tubes on the microscope stage to

flow culture medium. Culture media were flown at the rate of 10 ml/h for the first five minutes to remove the cells outside the growth channels, and at 2∼10 ml/h thereafter using a syringe pump (NE-1000, New Era Pump Systems) depending on the growth rate of the cells in each experimental condition. The high flow rates in the fast growth conditions were used for effectively removing cells from the device, not for changing the growth rates.

We used Nikon Ti-E microscope equipped with a thermostat chamber (TIZHB, Tokai Hit), 100x oil immersion objective (PlanFluor, N.A. 1.30, Nikon, or Plan Apo λ, N.A. 1.45, Nikon), cooled CCD camera (ORCA-R2, Hamamatsu Photonics), and LED excitation light source (DC2100, Thorlabs). The microscope was controlled by micromanager (https://micro-manager.org/). Before starting time-lapse, we let the cells in the growth channels grow until they filled the channels to ensure a constant environment from the beginning of the measurements. We selected 5-20 growth channels to track simultaneously in the time-lapse. The time-lapse intervals were changed depending on the growth conditions; we set the interval so that approximately 50 time points are included per mean generation time, which ranged from 30 sec - 3 min. The exposure time of excitation light was adjusted depending on the mean fluorescence intensity of the samples, which ranged from 100 - 2,000 msec.

Methods to estimate growth parameters

Population growth rate is determined by counting the number of cell divisions at time t ($N(t)$) and the number of cells that divided between t and $t+\Delta t$ ($D(t)$), where Δt is time-lapse interval, and by calculating $\Lambda_p = \frac{1}{n\Delta t}\sum_{i=0}^{n-1} \ln\left(\frac{N(i\Delta t)+D(i\Delta t)}{N(i\Delta t)}\right)$, where n is the number of time-points in the measurements. To evaluate the error ranges, we utilized a bootstrapping method, in which the number of cell division events between t and $t+\Delta t$ is determined by $N(t)$ trials of division with the probability of $D(t)/N(t)$. The same procedure was done for all the time points and population growth rate was calculated for the produced dataset in each cycle. By repeating the resampling and the evaluation 10,000 cycles, the error ranges were evaluated by (mean) ± (2 standard deviation) or 95% confidence interval of the resampled values.

The generation time distribution is related to the age-specific division rate $b(\tau)$ by $g(\tau) = b(\tau)\exp\left[-\int_0^\tau b(\tau')d\tau'\right]$ (SI Appendix Table S4). We measured the age-specific division rate from the single-cell data using $b(\tau) = \frac{-1}{\Delta t}\ln\left(\frac{N_a(\tau)-D_a(\tau)}{N_a(\tau)}\right)$, where $N_a(\tau)$ is the number of cells that reached age τ, and $D_a(\tau)$ is the number of cells that divided between age τ and $\tau+\Delta t$. We determined the generation time distribution $g(\tau)$ and the mean and the variance of generation time as explained in the simulation section below. The errors of the growth parameters associated with generation time were also estimated in a bootstrap manner, in which the number of cell divisions at age τ is determined by $N_a(\tau)$ trials of division with the probability of $D_a(\tau)/N_a(\tau)$. The same procedure was done for all ages and the mean and variance of generation time were calculated from the produced dataset in each cycle. By repeating this resampling 10,000 cycles, we evaluated the error ranges of the parameters by (mean) ± (2 standard deviation) or by 95% confidence interval.

We confirmed by simulation that these estimators provide precise measures of population growth rate and generation time distributions both with and without cell removal as explained below (SI Appendix Fig. S6-S10). The values of the measurement results on the growth parameters are shown in SI Appendix Table S1.

THEORY AND SIMULATION

Theory of age-structured population model

Model setting Below we derive several mathematical relations that interconnect growth parameters based on a simple age-structured population model (Figure 3D). The more detailed and mathematically rigorous derivations can be found in [7, 8, 9].

Here we assume that cells simply divide probabilistically accoroding to age-specific division probability $b(\tau)\delta\tau$, where τ is age (= time elapsed since previous division) (Figure 3D). $b(\tau)$ is called *hazard function* in the context of survival analysis [10]. The probability for a newborn cell to stay undivided until age $\tau = n\delta\tau$ $(n = 0, 1, 2, \cdots)$ is

$$B(\tau) = \prod_{i=0}^{n-1}(1 - b(i\delta\tau)\delta\tau) \approx \prod_{i=0}^{n-1} e^{-b(i\delta\tau)\delta\tau} = e^{-\sum_{i=0}^{n-1} b(i\delta\tau)\delta\tau} \longrightarrow e^{-\int_0^\tau b(\tau')d\tau'} \ (\delta\tau \to 0). \quad (1)$$

Let $g(\tau)\delta\tau$ be the probability for a newborn cell to divide at age τ ($g(\tau)$ is called (cellular) generation time distribution). By definition, $g(\tau)\delta\tau = B(\tau) \cdot b(\tau)\delta\tau$. Therefore,

$$g(\tau) = b(\tau)B(\tau) = -\frac{dB(\tau)}{d\tau} \quad (2)$$

from (1). $b(\tau)$, $B(\tau)$, and $g(\tau)$ are equivalent in terms that knowing one of them allows the derivation of the other two by the relations in SI Appendix Table S4.

An important growth parameter, mean generation time $\langle\tau\rangle_g = \int_0^\infty \tau g(\tau)d\tau$, is given directly from $B(\tau)$ as

$$\langle\tau\rangle_g = \int_0^\infty B(\tau)d\tau. \quad (3)$$

Moreover, the variance of generation time is also given by

$$V_g = \langle\tau^2\rangle_g - \langle\tau\rangle_g^2 = 2\int_0^\infty \tau B(\tau)d\tau - \left(\int_0^\infty B(\tau)d\tau\right)^2. \quad (4)$$

As explained below, we utilized these relations to estimate the means and the variances of generation time in the data analysis.

Population growth rate and age distribution Consider an exponentially growing cell population in which all the members grow and divide according to the scheme in Figure 3D. We assume that the environment is constant and $b(\tau)$ is unchanged over the time-course as well as among the cells. The growth rate and age distribution of population eventually converge to a constant value and stationary distribution after a sufficiently long time.

Let $\psi_p(\tau)$ be stationary age distribution of population, and $N(t)$ be the number of cells in the population at time t. The number of cells whose age falls into the fraction $[\tau, \tau + \delta\tau]$ at time t is $N(t)\psi_p(\tau)\delta\tau$. Among them, $N(t)\psi_p(\tau)\delta\tau \cdot (1 - b(\tau)\delta\tau)$ cells will constitute the age fraction $[\tau + \delta t, \tau + \delta\tau + \delta t]$ at time $t + \delta t$. Therefore,

$$\psi_p(\tau + \delta t)\delta\tau = \frac{N(t)\psi_p(\tau)\delta\tau \cdot (1 - b(\tau)\delta t)}{N(t + \delta t)}. \quad (5)$$

The denominator reflects the increase of cell number in the population by proliferation. When Λ_p is population growth rate,

$$N(t + \delta t) = N(t)e^{\Lambda_p \delta t} \approx N(t)(1 + \Lambda_p \delta t). \quad (6)$$

From (5) and (6), we obtain

$$\frac{d\psi_p(\tau)}{d\tau} = -(b(\tau) + \Lambda_p)\psi_p(\tau).$$

Solving this equation finds

$$\psi_p(\tau) = Ce^{-\Lambda_p \tau} e^{-\int_0^\tau b(\tau')d\tau'} = Ce^{-\Lambda_p \tau} B(\tau), \tag{7}$$

where C is a constant.

Next we determine C. Among $N(t)$ cells at time t, $N(t)\left(\int_0^\infty \psi_p(\tau)b(\tau)d\tau\right)\delta t$ cells divide by $t+\delta t$, and constitute $\psi_p(0)\delta t$ fraction at time $t+\delta t$. Therefore,

$$N(t+\delta t) = N(t) + N(t)\left(\int_0^\infty \psi_p(\tau)b(\tau)d\tau\right)\delta t = N(t)\left\{1 + \left(\int_0^\infty \psi_p(\tau)b(\tau)d\tau\right)\delta t\right\}, \tag{8}$$

and

$$\psi_p(0)\delta t = \frac{2N(t)\left(\int_0^\infty \psi_p(\tau)b(\tau)d\tau\right)\delta t}{N(t+\delta t)}. \tag{9}$$

The factor 2 in (9) comes from the fact that each division produces two cells with age=0. From (6) and (8),

$$\Lambda_p = \int_0^\infty \psi_p(\tau)b(\tau)d\tau. \tag{10}$$

Hence, from (9),

$$\psi_p(0) = 2\Lambda_p. \tag{11}$$

From (7) and (11), we obtain

$$\psi_p(\tau) = 2\Lambda_p e^{-\Lambda_p \tau} B(\tau). \tag{12}$$

The population growth rate Λ_p can be determined from $B(\tau)$ because $\psi_p(\tau)$ must satisfy $\int_0^\infty \psi_p(\tau)d\tau = 1$. Thus, from (12), an important relation is derived:

$$\int_0^\infty e^{-\Lambda_p \tau} B(\tau)d\tau = \frac{1}{2\Lambda_p}. \tag{13}$$

Also, inserting (12) into (10) finds

$$\int_0^\infty 2g(\tau)e^{-\Lambda_p \tau}d\tau = 1, \tag{14}$$

which is called the Euler-Lotka equation [11]. The equations (13) and (14) allow the calculation of population growth rate Λ_p from the information of generation time distribution ($B(\tau)$ or $g(\tau)$) at least numerically. Thus, generation time distribution uniquely determines the stationary age distribution $\psi_p(\tau)$ by (12).

The Euler-Lotka equation (14) is analytically solvable only in the limited cases. When $g(\tau)$ is gamma distribution (i.e., $g(\tau) = \frac{\tau^{k-1}e^{-\frac{\tau}{\theta}}}{\Gamma(k)\theta^k}$, where $k(>0)$ is shape parameter, $\theta(>0)$ is scale parameter, and $\Gamma(\cdot)$ is gamma function), we can find the anlytical solution as

$$\Lambda_p = \frac{2^{\frac{1}{k}} - 1}{\theta}.$$

Therefore,

$$T_d = \frac{\theta \log 2}{2^{\frac{1}{k}} - 1}.$$

By defining single-cell growth rate as $\lambda \equiv \frac{\log 2}{\langle\tau\rangle_g}$, we introduce *growth rate gain* as

$$\frac{\Lambda_p - \lambda}{\lambda} = \frac{\langle\tau\rangle_g - T_d}{T_d}.$$

In the case where $g(\tau)$ is gamma, the growth rate gain is

$$\begin{aligned}\frac{\langle\tau\rangle_g - T_d}{T_d} &= \frac{k\theta - \frac{\theta\log 2}{2^{\frac{1}{k}}-1}}{\frac{\theta\log 2}{2^{\frac{1}{k}}-1}} \\ &= \frac{k\left(2^{\frac{1}{k}}-1\right)}{\log 2} - 1. \end{aligned} \tag{15}$$

Since $2^{\frac{1}{k}} = e^{\frac{\log 2}{k}} = 1 + \left(\frac{\log 2}{k}\right) + \frac{1}{2!}\left(\frac{\log 2}{k}\right)^2 + \cdots$,

$$\frac{\langle\tau\rangle_g - T_d}{T_d} = \sum_{i=1}^{\infty} \frac{1}{(i+1)!}\left(\frac{\log 2}{k}\right)^i. \tag{16}$$

The right-hand side of (16) is positive. Thus, the population doubling time is smaller than the mean generation time. In fact, the positivity of growth rate gain is proven generally true even when $g(\tau)$ is not gamma, as shown below.

The coefficient of variation (η) of gamma distribution is $\sqrt{\frac{1}{k}}$. Therefore, from (15) and (16),

$$\frac{\langle\tau\rangle_g - T_d}{T_d} = \frac{2^{\eta^2}-1}{\eta^2\log 2} - 1 = \sum_{i=1}^{\infty}\frac{(\log 2)^i}{(i+1)!}\eta^{2i}.$$

Hence, the growth rate gain is determined solely by CV when $g(\tau)$ is gamma.

Inequality between mean generation time and population doubling time The Euler-Lotka equation (14) indicates that

$$g^*(\tau) = 2g(\tau)e^{-\Lambda_p\tau} \tag{17}$$

is also a probability density function (we explain below that $g^*(\tau)$ has its own meanings). Based on this fact, one can show that population doubling time $T_d = \frac{\log 2}{\Lambda_p}$ (= time required for the population to double the number of cells) is smaller than mean generation time $\langle\tau\rangle_g$.

From (17),

$$\begin{aligned}\frac{e^{\Lambda_p\tau}}{2} &= \frac{g(\tau)}{g^*(\tau)} \\ \Lambda_p\tau\log_2 e - 1 &= \log_2\frac{g(\tau)}{g^*(\tau)}. \end{aligned} \tag{18}$$

Multiplying both sides by $g(\tau)$ and integrating from zero to infinity finds

$$\Lambda_p\langle\tau\rangle_g\log_2 e - 1 = D[g||g^*],$$

where $D[g||g^*] \equiv \int_0^\infty g(\tau)\log_2\frac{g(\tau)}{g^*(\tau)}d\tau$ is the Kullback-Leibler divergence, which is always non-negative [12]. Since $\Lambda_p\log_2 e = \frac{1}{T_d}$,

$$\frac{\langle\tau\rangle_g - T_d}{T_d} = D[g||g^*] \geq 0. \tag{19}$$

The equality holds when $g^*(\tau) = g(\tau)$. This condition is satisfied only when $g(\tau) = \delta(\tau - \langle\tau\rangle_g)$. Therefore, population doubling time is strictly lower than mean generation time for any realistic case in which variability of cell division times is observed.

In a similar manner, we can show that the mean of $g^*(\tau)$ is smaller than T_d: Multiplying the both-hand sides of (18) by $-g^*(\tau)$ and integrating from zero to infinity finds

$$1 - \Lambda_p \langle \tau \rangle_{g^*} \log_2 e = D[g^*||g].$$

Therefore,

$$\frac{T_d - \langle \tau \rangle_{g^*}}{T_d} = D[g^*||g] \geq 0. \tag{20}$$

From (19) and (20),

$$\frac{\langle \tau \rangle_g - \langle \tau \rangle_{g^*}}{T_d} = D[g||g^*] + D[g^*||g] \geq 0.$$

Based on these relations, we can understand the order of the growth parameters: $\langle \tau \rangle_{g^*} \leq T_d \leq \langle \tau \rangle_g$.

Ancestral generation time distribution The function $g^*(\tau)$ represents the *ancestral generation time distribution*, i.e. probability density function of the parental cell's generation time in a population.

Let $N(t)$ be the number of cells at time t in a population growing at a constant rate Λ_p. We assume $N(t)$ is sufficiently large. The cells at age τ' at time t originated from the parental cells that divided at time $t - \tau'$ among $N(t - \tau') = N(t)e^{-\Lambda_p \tau'}$ cells. The number of cells that divided at $t - \tau'$ at age τ is $N(t - \tau')\psi_p(\tau)b(\tau)\delta\tau$, and $2N(t - \tau')\psi_p(\tau)b(\tau)\delta\tau$ newborn cells are produced. Among them, $2N(t - \tau')\psi_p(\tau)b(\tau)\delta\tau \cdot B(\tau')$ cells reach age τ' at time t. Therefore, the probability that the generation time of a parental cell becomes τ is

$$g_p(\tau)\delta\tau = \frac{\int_0^\infty 2N(t - \tau')\psi_p(\tau)b(\tau)\delta\tau \cdot B(\tau')d\tau'}{N(t)}.$$

Thus,

$$\begin{aligned} g_p(\tau) &= \int_0^\infty 2e^{-\Lambda_p \tau'} \cdot 2\Lambda_p e^{-\Lambda_p \tau} B(\tau)b(\tau)B(\tau')d\tau' \\ &= 4\Lambda_p g(\tau)e^{-\Lambda_p \tau} \int_0^\infty e^{-\Lambda_p \tau'} B(\tau')d\tau' \\ &= 2g(\tau)e^{-\Lambda_p \tau}, \end{aligned}$$

which is equivalent of $g^*(\tau)$ (17). To obtain the final result, we utilized the relation (13).

Generation time distributions along cell lineages Next we consider generation time distributions along two types of cell lineages. In one situation, we obtain a lineage by tracking a single cell in isolation in the time-forward manner, selecting just one of the two sibling cells randomly at every cell division. See refs [13, 14] for the experimental realization of such tracking method. This type of cell lineage can be also obtained by mother machine [15] when mother-daughter distinction is negligible. If a lineage obtained in this manner is sufficiently long, the empirical distribution of generation time along the lineage should converge to $g(\tau)$.

In the other situation, we extract a lineage from a population, i.e. selecting a cell in a population and tracking back along its past history over many generations. A lineage extracted in this manner is called a time-backward, retrospective, or time-reversed history in the literatures [16, 17, 18]. In this case, the probability that the generation time of the parental cell of the selected cell becomes τ is $g_p(\tau)\delta\tau$. This is also true for all the ancestral cells on this lineage. Thus, the empirical distribution of generation time along the lineage obtained in this manner should converge to $g_p(\tau) = g^*(\tau)$ instead of $g(\tau)$.

Since $g(\tau)$ and $g^*(\tau)$ can be understood as the typical generation time distributions along the lineages in isolation and within a population, respectively, (19) shows that the relative difference

between the mean generation time and the population doubling time, $\frac{\langle\tau\rangle_g - T_d}{T_d}$, is directly related to the different statistics of generation time along those two lineage types. The difference between $g(\tau)$ and $g^*(\tau)$ comes from the fact that the descendant cells of the fast dividing cells tend to be over-represented in the population (Figure 1).

In our previous study, we derived $g^*(\tau)$ based on path integrals and a variational optimization principle and called the lineages with $g^*(\tau)$ *optimal* [9]. The path integral viewpoint is in fact quite powerful, providing the conceptual understanding as to why the lineages with $g^*(\tau)$ are optimal, and makes the connection with evolutionary selection: the age distribution along the optimal lineages, $\rho^*(\tau) = \frac{1}{\langle\tau\rangle_{g^*}} \int_\tau^\infty g^*(\tau')d\tau'$, directly reports the strength of selection acting at each age. Thus, $g^*(\tau)$ itself has a clear biological meaning.

Simulation test for the precision of growth parameter estimators

As described in the main text, we calculated population growth rate (doubling time) and mean generation time from the lineage tree structures (e.g. Fig. 2D and SI Appendix Fig. S4). Below we explain how we estimated those growth parameters from the data, and confirm the precision of the estimators by simulation.

Simulation setting To evaluate the precision of the estimators for the growth parameters, we produced the artificial datasets of cell proliferation by simulation in which all the cells divide probabilistically in an age-dependent manner according to the scheme in Figure 3D. Three cases of generation time distribution were tested in the simulation (SI Appendix Fig. S6A-C):

(Case A) Gamma distribution ($\langle\tau\rangle_g = 50$, $V_g = 400$)

$$g(\tau) = \frac{\tau^{k-1}e^{-\frac{\tau}{\theta}}}{\Gamma(k)\theta^k}, \qquad k = \frac{50}{8}, \quad \theta = 8,$$

($\Gamma(k)$ is gamma function).

(Case B) Gamma distribution with large variance ($\langle\tau\rangle_g = 50$, $V_g = 800$)

$$g(\tau) = \frac{\tau^{k-1}e^{-\frac{\tau}{\theta}}}{\Gamma(k)\theta^k}, \qquad k = \frac{50}{16}, \quad \theta = 16.$$

(Case C) Shifted gamma distribution ($\langle\tau\rangle_g = 50$, $V_g = 400$)

$$g(\tau) = \begin{cases} 0 & (\tau < a) \\ \frac{(\tau-a)^{k-1}e^{-\frac{\tau-a}{\theta}}}{\Gamma(k)\theta^k} & (\tau \geq a) \end{cases}, \qquad k = 4, \quad \theta = 10, \quad a = 10.$$

Gamma and shifted gamma distributions are often used to approximate the real generation time distributions [8, 9], though neither of them consistently agreed with all the experimental distributions we obtained.

By fixing the distribution type to gamma or shifted gamma, we can easily calculate population growth rate from the Euler-Lotka equation (14): For gamma distribution,

$$\Lambda_p = \frac{2^{\frac{1}{k}} - 1}{\theta};$$

and for shifted gamma distribution, Λ_p is the single positive root of

$$2e^{-\Lambda_p a}\left(1 + \Lambda_p\theta\right)^{-k} = 1.$$

In the three cases above, population doubling times ($T_d = \frac{\ln 2}{\Lambda_p}$) in arbitral time unit (a.t.u.) are 47.279 (Case 1), 44.660 (Case 2), and 47.329 (Case 3), respectively, which are all smaller than the mean generation time ($\langle\tau\rangle_g = 50$). Good estimators must retrieve those pre-assigned values from the simulation datasets.

Population growth rate Population growth rate Λ_p is usually evaluated as the slope of a growth curve in the semi-log plot for an exponentially growing cell population (Figure 1C). Here we denote the growth rate estimator calculated in this manner as $\hat{\Lambda}_p^{(1)}$. Although the estimator $\hat{\Lambda}_p^{(1)}$ is simple and straightforward, it cannot be applied to a cell population in dynamics cytometer because a part of the cells in this device are constantly removed. Instead of $\hat{\Lambda}_p^{(1)}$, we can also estimate population growth rate by directly counting the division events in a population, which is feasible in the single-cell measurements.

Let $N(t)$ and $D^{(\delta t)}(t)$ be the numbers of cells at time t and of cells that divided between t and $t+\delta t$, respectively. Note that $N(t+\delta t) = N(t) + D^{(\delta t)}(t)$ when no cell is removed from the population. We can introduce *instantaneous division rate*, which satisfies $N(t) + D^{(\delta t)}(t) = N(t)e^{\hat{\Lambda}^{(\delta t)}(t)\delta t}$. Therefore,

$$\hat{\Lambda}^{(\delta t)}(t) = \frac{1}{\delta t}\log\left(\frac{N(t) + D^{(\delta t)}(t)}{N(t)}\right).$$

For balanced-growth cultures, $\hat{\Lambda}^{(\delta t)}(t)$ must be nearly constant over the time-course. Hence the mean of $\Lambda^{(\delta t)}(t)$ is expected to give the correct population growth rate. Thus, we defined a new population growth rate estimator $\hat{\Lambda}_p^{(2)}$ as

$$\hat{\Lambda}_p^{(2)} = \langle\hat{\Lambda}^{(\Delta t)}\rangle = \frac{1}{n\Delta t}\sum_{i=0}^{n-1}\log\left(\frac{N(i\Delta t) + D^{(\Delta t)}(i\Delta t)}{N(i\Delta t)}\right), \tag{21}$$

where n is the number of time points in the single-cell time-lapse measurement, and Δt is the time-lapse interval. $\hat{\Lambda}_p^{(2)}$ has an advantage over $\hat{\Lambda}_p^{(1)}$ because it is applicable even with cell removal provided that the number of cells removed at each time point is small relative to the total population size; we show below how the precision of $\hat{\Lambda}_p^{(2)}$ is altered depending on population size $N(t)$.

Evaluation of population growth rate estimators by simulation (without cell removal) First, we consider growing cell populations without cell removal like standard single-cell time-lapse microscopy on agarose pad (see [19] for example). To evaluate the precision of the estimators under experimentally realistic conditions, we produced 20 lineage trees per one cycle for the duration of 6× mean generation time (i.e. $T_L = 300$ a.t.u.). Each tree is orignated from a single cell whose age at $t = 0$ was determined by the expected population age distributions. For each cycle of simulation, we calculated $\hat{T}_d^{(1)} = \frac{\ln 2}{\hat{\Lambda}_p^{(1)}}$ and $\hat{T}_d^{(2)} = \frac{\ln 2}{\hat{\Lambda}_p^{(2)}}$ by assuming the time-lapse interval $\Delta t = 1$ a.t.u., and evaluated the error ranges by repeating the simulation in 1,000 cycles.

The results show that the both $\hat{\Lambda}_p^{(1)}$ and $\hat{\Lambda}_p^{(2)}$ correctly retrieved the population growth rates under all the distribution conditions (SI Appendix Fig. S6D-F). The error ranges of $\hat{T}_d^{(2)}$ were slightly larger than those of $\hat{T}_d^{(1)}$, though small enough to distinguish the difference between $\langle\tau\rangle_g$ and T_d. Therefore, the both estimators are usable for evaluating population growth rate in standard single-cell time-lapse microscopy.

Evaluation of population growth rate estimators by simulation (with cell removal) Next we consider a population proliferating in a similar setting of dynamics cytometer. We now assume that cells proliferate in growth channels aligned on an array (SI Appendix Fig. S7). Cells are stably harbored in the "safety section" in the middle of the growth channel. The length and the width of the growth channel determine the cell capacity of the safety section. In the simulation, we assumed that the division of a cell in the safety section places two newborn cells; one at the same position and the other at one of the neighboring positions in the channel.

Placement of a newborn cell at a different position move a part of the cells on the row toward the end of the growth channel as schematically explained in SI Appendix Fig. S7. Cells outside the safety section was removed at every time point from the analysis as done in the analysis on the experimental data.

We simulated cell proliferation processes for the duration of 100× mean generation time using the same three generation time distributions as above under diffrent conditions of cell capacity of the safety section. For each cycle of simulation, we produced the data of a single growth channel, and extracted the information of lineage tree assuming that $\Delta t = 1$ a.t.u. Then, we calculated $\hat{T}_d^{(2)}$.

The result showed that the precision of the estimator $\hat{T}_d^{(2)}$ depended on the number of cell in a row (N_R) in the safety section: When N_R is larger than $\sim$5, $\hat{T}_d^{(2)}$ reported correct population doubling time, though it underestimated the true value when N_R is less than $\sim$5 (SI Appendix Fig. S8). This reliability bound was robust against the different generation time conditions (SI Appendix Fig. S8).

In our experiment, $N_R = 8 \sim 10$, thus the population doubling time estimated by $\hat{T}_d^{(2)}$ is expected fairly precise.

Generation time distribution The simplest approach to estimate cellular generation time distribution from lineage trees is sampling all the "measurable" generation times in the tree, which is however apparently inappropriate because smaller generation times are inevitably over-represented in the samples. To avoid this bias, we can instead estimate age-specific division rate $b(\tau)$, which allows us to retrieve the information of generation time distributions (SI Appendix Table S4).

Let $N_a(\tau)$ and $D_a^{(\delta\tau)}(\tau)$ be the numbers of cells at age τ and of cells that divided between age τ and $\tau+\delta\tau$, respectively. The number of cells at age $\tau+\delta\tau$ is thus $N_a(\tau+\delta\tau) = N_a(\tau) - D_a^{(\delta\tau)}(\tau)$ when no cells are removed from the population. Here we introduce age-specific division rate $b(\tau)$, which satisfies $N_a(\tau) - D_a^{(\delta\tau)}(\tau) = N_a(\tau)e^{-b(\tau)\delta\tau}$. Therefore,

$$b(\tau) = -\frac{1}{\delta\tau}\log\left(\frac{N_a(\tau) - D_a^{(\delta\tau)}(\tau)}{N_a(\tau)}\right).$$

Note that $N_a(\tau)$ and $D_a^{(\delta\tau)}(\tau)$ are obtainable from lineage trees. In the actual analysis on the experimental data, we estimated age-specific division rate at age $i\Delta t$ ($i = 0, 1, 2, \cdots$) by

$$\hat{b}(i\Delta t) = -\frac{1}{\Delta t}\log\left(\frac{N_a(i\Delta t) - D_a^{(\Delta t)}(i\Delta t)}{N_a(i\Delta t)}\right),$$

where Δt is the time-lapse interval.

Based on the relation (1), we estimated $B(\tau)$ (survival function of $g(\tau)$) as

$$\hat{B}(i\Delta t) = \begin{cases} \exp\left[-\sum_{j=0}^{i-1}\hat{b}(j\Delta t)\Delta t\right] & (i \geq 1) \\ 1 & (i = 0) \end{cases}, \tag{22}$$

and mean generation time as

$$\langle\hat{\tau}\rangle_g^{(1)} = \sum_i \hat{B}(i\Delta t)\Delta t, \tag{23}$$

from the relation (3).

SI Appendix Fig. S9 confirms that $\hat{B}(\tau)$ correctly retrieves the survival function of pre-assigned generation time distributions. The probability density function $g(\tau)$ is related to $B(\tau)$

by (2). Therefore, the probability for a generation time to fall into the interval $[\tau, \tau + \Delta\tau)$ is $\int_{\tau}^{\tau+\Delta\tau} g(\tau')d\tau' = B(\tau) - B(\tau + \Delta\tau)$. From this relation, we estimated the histogram of $g(\tau)$ by

$$\hat{h}_g(i\Delta\tau, (i+1)\Delta\tau) = \hat{B}(i\Delta\tau) - \hat{B}((i+1)\Delta\tau), \tag{24}$$

where $\Delta\tau$ is the bin size of the histogram. This estimator was used to obtain the histograms in Fig. 2A and Extended Data Fig. 11.

Evaluation of generation time estimators by simulation We evaluated the precision of the estimators $\hat{B}(\tau)$ and $\langle\hat{\tau}\rangle_g^{(1)}$ using the simulation datasets produced above for population growth rate. The results confirmed that these estimators were precise in the both cases of with/without cell removal, irrespectively of generation types (SI Appendix Fig. S6, S8, and S9). We also confirmed that the simple sample means of all the measurable generation times in lineage trees, which we denote $\langle\hat{\tau}\rangle_g^{(2)}$, are biased, being much smaller than the true values (SI Appendix Fig. S6 and S8). $\langle\hat{\tau}\rangle_g^{(2)}$ is close to $\langle\tau\rangle_{g^*}$; it is understandable because $\langle\hat{\tau}\rangle_g^{(2)}$ in fact evaluates the mean of ancestral generation time distribution, which is equivalent of $g^*(\tau)$ as shown above.

Estimator for variance of generation time The variance of generation time can be calculated directly from $B(\tau)$ by (4). Based on this relation, we searched for an appropriate estimator for V_g, finding that

$$\hat{V}_g^{(1)} = 2\left[\sum_{i=0}^{i_{max}} \left\{\left(i + \frac{1}{2}\right)\Delta t\right\} \hat{B}(i+1)\right] - \left(\langle\hat{\tau}\rangle_g^{(1)} - \Delta t\right)^2 \tag{25}$$

correctly reports the pre-assigned values of variance in all the settings of the simulation (SI Appendix Fig. S10, $i_{max}\Delta t$ is the maximum age observed in a lineage tree). We used this estimator in the analysis of the experimental data (Figure 6 in the main text). In SI Appendix Fig. S10, we also show the values of the estimator

$$\hat{V}_g^{(2)} = 2\left[\sum_{i=0}^{i_{max}} \left\{\left(i + \frac{1}{2}\right)\Delta t\right\} \hat{B}(i+1)\right] - \left(\langle\hat{\tau}\rangle_g^{(1)}\right)^2, \tag{26}$$

whose definition is more straightforward than that of $\hat{V_g^{(1)}}$ from (4), but significantly underestimated the true values.

Theoretical prediction of population growth rate from generation time distribution When the age-structured population model in Figure 3D is valid, generation time distribution uniquely determines population growth rate by the Euler-Lotka equation (14). Equivalently, we can also determine population growth rate from survival function $B(\tau)$ based on the relation (13).

We predicted population growth rate Λ_p and doubling time T_d from the estimator $\hat{B}(\tau)$ by numerically searching for the root of

$$\Lambda_p \sum_{j=0}^{i_{max}-1} \frac{\hat{B}(j\Delta t) + \hat{B}((j+1)\Delta t)}{2} e^{-\Lambda_p \cdot j\Delta t} = \frac{1}{2},$$

where $i_{max}\Delta t$ is the maximum age observed in a lineage tree. We denoted the population growth rate estimator calculated in this way as $\hat{\Lambda}_p^{(th)}$ (doubling time, $\hat{T}_d^{(th)} = \frac{\log 2}{\hat{\Lambda_p}^{(th)}}$).

The application of the estimators to the simulation datasets showed that $\hat{T}_d^{(th)}$ retrieved the correct population doubling times under all the simulation conditions (SI Appendix Fig. S6D-F

and S8). The precision of the estimator was unaltered by the difference of with/without cell removal. Therefore, it is conceivable that the estimator $\hat{T}_d^{(th)}$ can predict the correct population doubling times as long as the real cell populations follow the proliferation scheme in Figure 3D.

Theoretical prediction of population age distribution from generation time distribution When cells follow the proliferation scheme in Figure 3D, generation time distribution of single cells uniquely determines population age distribution by (12). From this, we calculated *theoretically estimated population age distribution* by

$$\hat{\psi}_p^{(th)}(i\Delta t) = 2\hat{\Lambda}_p^{(th)} e^{-\hat{\Lambda}_p^{(th)}(i\Delta t)} \hat{B}(i\Delta t).$$

Note that $\hat{\psi}_p^{(th)}(i\Delta t)$ is uniquely calculated only from the information of single-cell lineage trees and time-lapse interval with no assumption on distribution type for generation time.

Application of the estimators to experimental data SI Appendix Table S1 shows the single-cell growth rates measured by $\hat{\lambda}^{(1)} \equiv \frac{\ln 2}{\langle \hat{\tau} \rangle_g^{(1)}}$ and $\hat{\lambda}^{(2)} \equiv \frac{\ln 2}{\langle \hat{\tau} \rangle_g^{(2)}}$ compared with population growth rates measured by $\hat{\Lambda}_p^{(2)}$, using the actual experimental data. Comparison between the validated single-cell growth rate estimator $\hat{\lambda}^{(1)}$ and population growth rate estimator $\hat{\Lambda}_p^{(2)}$ confirms that population can grow faster than single cells on average under most conditions.

We also show the mean elongation rates ($\hat{\mu}_r$) in SI Appendix Table S1. Elongation rate is obtained by fitting an exponential curve to a cell size elongation curve of an individual cell, and its mean among cells in a population is often used as a proxy of population growth rate in many single-cell studies. Here, the estimator $\hat{\mu}_r$ denotes the mean of elongation rates from all the cells in the lineage trees whose full generation data were obtained (i.e., cells at the very beginning of the lineage trees and those removed from the growth channels before division were excluded). The result shows that $\hat{\mu}_r$ is significantly deviated from $\hat{\Lambda}_p^{(2)}$ in most cases, which indicates that mean elongation rate is not a suitable measure of population growth rate.

References

[1] Merrin J, Leibler S, Chuang JS (2007) Printing multistrain bacterial patterns with a piezoelectric inkjet printer. PLoS One 2(7):e663.

[2] Zaslaver A, et al. (2006) A comprehensive library of fluorescent transcriptional reporters for Escherichia coli. Nat Methods 3(8):6238.

[3] Zaslaver A, et al. (2009) Invariant distribution of promoter activities in Escherichia coli. PLoS Comput Biol 5(10):e1000545.

[4] Lutz R, Bujard H (1997) Independent and tight regulation of transcriptional units in Escherichia coli via the LacR/O, the TetR/O and AraC/I1-I2 regulatory elements. Nucleic Acids Res 25(6):120310.

[5] Datsenko KA, Wanner BL (2000) One-step inactivation of chromosomal genes in Escherichia coli K-12 using PCR products. Proc Natl Acad Sci U S A 97(12):66405.

[6] Nagai T, et al. (2002) A variant of yellow fluorescent protein with fast and efficient maturation for cell-biological applications. Nat Biotechnol 20(1):8790.

[7] Bellman R, Harris TE (1948) On the theory of age-dependent stochastic branching processes. Proc Natl Acad Sci U S A 34(12):601-4.

[8] Powell EO (1956) Growth rate and generation time of bacteria, with special reference to continuous culture. J Gen Microbiol 15(3):492-511.

[9] Wakamoto Y, Grosberg AY, Kussell E (2012) Optimal lineage principle for age-structured populations. Evolution 66(1):115-34.

[10] Kleinbaum DG, Klein M (2005) Survival Analysis: A Self-Learning Text (Springer Science & Business Media).

[11] Charlesworth B (2000) Fisher, Medawar, Hamilton and the evolution of aging. Genetics 156(3):927-31.

[12] Cover TM, Thomas JA (2006) Elements of Information Theory (Wiley).

[13] Wakamoto Y, Umehara S, Matsumura K, Inoue I, Yasuda K (2003) Development of non-destructive, non-contact single-cell based differential cell assay using on-chip microcultivation and optical tweezers. Sensors Actuators B Chem 96(3):693-700.

[14] Wakamoto Y, Ramsden J, Yasuda K (2005) Single-cell growth and division dynamics showing epigenetic correlations. Analyst 130(3):311-7.

[15] Wang P, et al. (2010) Robust growth of Escherichia coli. Curr Biol 20(12):1099-103.

[16] Sughiyama Y, Kobayashi TJ, Tsumura K, Aihara K (2015) Pathwise thermodynamic structure in population dynamics. Phys Rev E 91:032120.

[17] Hermisson J, Redner O, Wagner H, Baake E (2002) Mutation-selection balance: ancestry, load, and maximum principle. Theor Popul Biol 62(1):9-46.

[18] Mustonen V, Lässig M (2010) Fitness flux and ubiquity of adaptive evolution. Proc Natl Acad Sci U S A 107(9):4248-53.

[19] Stewart EJ, Madden R, Paul G, Taddei F (2005) Aging and death in an organism that reproduces by morphologically symmetric division. PLoS Biol 3(2):e45.

Supplemental Tables

Table S1: Growth Rate Estimates from the Experimental Data. $\hat{\lambda}^{(1)} = \frac{\log 2}{\langle \hat{\tau} \rangle_g^{(1)}}$, and $\hat{\lambda}^{(2)} = \frac{\log 2}{\langle \hat{\tau} \rangle_g^{(2)}}$. $\hat{\mu}_r^{(2)}$ is the mean of elongation rate of the cells which were born and reached the next division in the lineage trees. The unit is 10^{-3} min^{-1}. The error ranges are 95% bootstrap confidence interval.

Strain	Conditions	$\hat{\lambda}^{(1)}$	$\hat{\Lambda}_p^{(2)}$	$\hat{\lambda}^{(2)}$	$\hat{\mu}_r^{(2)}$
F3 rpsL-gfp	M9 cas. acids, 37°C	26.4 (25.9 - 26.8)	27.1 (26.5 - 27.8)	29.4 (28.9 - 30.0)	27.3 (27.2 - 27.5)
	M9 LB, 37°C	23.8 (23.4 - 24.3)	24.7 (24.4 - 25.2)	26.5 (25.8 - 27.1)	27.3 (25.6 - 29.6)
	M9 glucose, 37°C	12.4 (12.2 - 12.7)	13.6 (13.1 - 14.1)	14.8 (14.6 - 15.0)	14.0 (13.9 - 14.2)
	M9 glucose, 30°C	6.60 (6.46 - 6.74)	7.05 (6.98 - 7.12)	8.22 (8.05 - 8.41)	7.79 (7.65 - 7.95)
	M9 glycerol, 37°C	4.09 (4.00 - 4.17)	4.24 (4.20 - 4.28)	5.03 (4.86 - 5.23)	4.41 (4.34 - 4.49)
	M9 glycerol, 30°C	4.49 (4.41 - 4.57)	4.69 (4.66 - 4.73)	5.37 (5.25 - 5.48)	5.02 (4.97 - 5.07)
F3 T7-venus	M9 glucose, 37°C	9.40 (9.25 - 9.54)	9.81 (9.74 - 9.88)	11.3 (11.1 - 11.4)	10.3 (10.2 - 10.3)
	M9 glucose, 30°C	5.28 (5.18 - 5.38)	5.57 (5.40 - 5.57)	6.03 (5.94 - 6.11)	5.72 (5.65 - 5.79)
F3 LVS	M9 glucose, 37°C	9.52 (9.26 - 9.77)	9.97 (9.85 - 10.1)	11.9 (11.6 - 12.1)	11.6 (11.4 - 11.7)
BrF2	M9 glucose, 37°C	20.9 (20.6 - 21.1)	20.9 (20.7 - 21.2)	22.0 (21.8 - 22.1)	22.1 (22.0 - 22.2)
	M9 glycerol, 37°C	10.9 (10.8 - 10.9)	11.0 (10.9 - 11.1)	11.5 (11.4 - 11.6)	11.6 (11.5 - 11.7)

Table S2: List of *E. coli* Strains Used in This Study.

Name	**Genotype**
F3 rpsL-gfp	W3110 Δ*fliC* Δ*fimA* Δ*flu* pUA66-rpsL
F3 T7-venus	W3110 Δ*fliC* Δ*fimA* Δ*flu* *lacZ*::T7RNAP *intC*::P$_{T7}$-*venus*
F3 LVS	W3110 Δ*fliC* Δ*fimA* Δ*flu* *intC*::P$_{LlacO-1}$-*venus-smR*
BrF2 rpsL-gfp	B/r Δ*fimA* Δ*flu* pUA66-rpsL

Table S3: List of Culture Media Used in This Study.

Name	**Composition**
M9 glucose	M9 base + 0.2% (w/w) glucose + 1/2 MEM amino acids solution
M9 glycerol	M9 base + 0.2% (w/w) glycerol
M9 casamino acids	M9 base + 0.2% (w/w) glucose + 1% (w/w) casamino acids
M9 LB	M9 base + 1% (w/w) LB medium + 1/2 MEM amino acids solution

Table S4: Relationships between $b(\tau)$, $B(\tau)$, and $g(\tau)$.

Input function	**Relations**
$b(\tau)$	$B(\tau) = e^{-\int_0^\tau b(\tau')d\tau'}$, $g(\tau) = b(\tau)e^{-\int_0^\tau b(\tau')d\tau'}$
$B(\tau)$	$b(\tau) = -\frac{d \log B(\tau)}{d\tau}$, $g(\tau) = -\frac{dB(\tau)}{d\tau}$
$g(\tau)$	$B(\tau) = \int_\tau^\infty g(\tau')d\tau'$, $b(\tau) = \frac{g(\tau)}{\int_\tau^\infty g(\tau')d\tau'}$

Table S5: Mother-Daughter Correlation of Generation Time.

Strain	Conditions	Correlation coefficient
F3 rpsL-gfp	M9 cas. acids, 37°C	-0.06 ± 0.03
	M9 LB, 37°C	-0.06 ± 0.04
	M9 glucose, 37°C	0.26 ± 0.02
	M9 glucose, 30°C	0.13 ± 0.03
	M9 glycerol, 37°C	0.08 ± 0.03
	M9 glycerol, 30°C	-0.08 ± 0.03
F3 T7-venus	M9 glucose, 37°C	0.08 ± 0.02
	M9 glucose, 30°C	0.02 ± 0.03
F3 LVS	M9 glucose, 37°C	0.11 ± 0.03
BrF2	M9 glucose, 37°C	-0.18 ± 0.03
	M9 glycerol, 37°C	0.02 ± 0.02

Supplemental movie

Movie S1. Time-lapse movie of BrF2 rpsL-gfp strain proliferating in a growth channel of dynamics cytometer. The culture condition of this experiment was M9 glycerol medium at 37°C. Bar, 5 μm.

Supplemental Figures

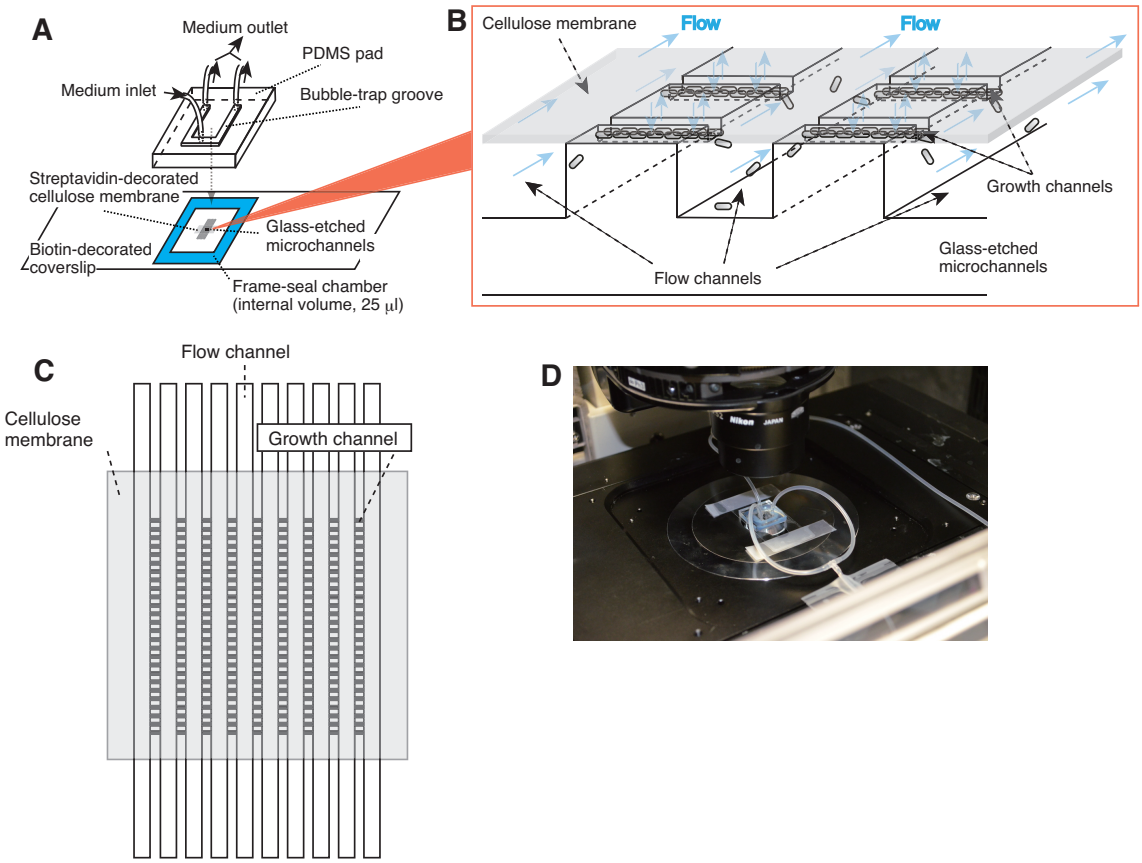

Figure S1: Additional Information on Dynamics Cytometer. A. Device assembly scheme. We created the microchannels directly on a glass coverslip by chemical etching. The surface of the coverslip was chemically decorated with biotin, which allowed sealing of the microchannel region by streptavidin-decorated cellulose membrane. To flow culture media, we attached PDMS pad on the coversilp via square frame-seal chamber (internal volume, 25 μl). The PDMS pad possesses one medium inlet, two outlets, and bubble trap groove. B. Bird-view scheme of the microchannels. Culture medium flows both in the flow channels and above the membrane to maintain the culture conditions around cells constant. C. The arrangement of microchannels and cellulose membrane. The dimension of one flow channel is 2000 μm (l)$\times$50 μm (w)$\times$ 15 μm (d), and that of growth channel is 30 μm (l)$\times$ 3 μm (w)$\times$1 μm (d), placed perpendicular to the flow channels on an array. The central part of the microchannel region is covered by cellulose membrane with the both ends of the flow channels left open to introduce medium in the flow channels. D. A photo of the device mounted on microscope stage.

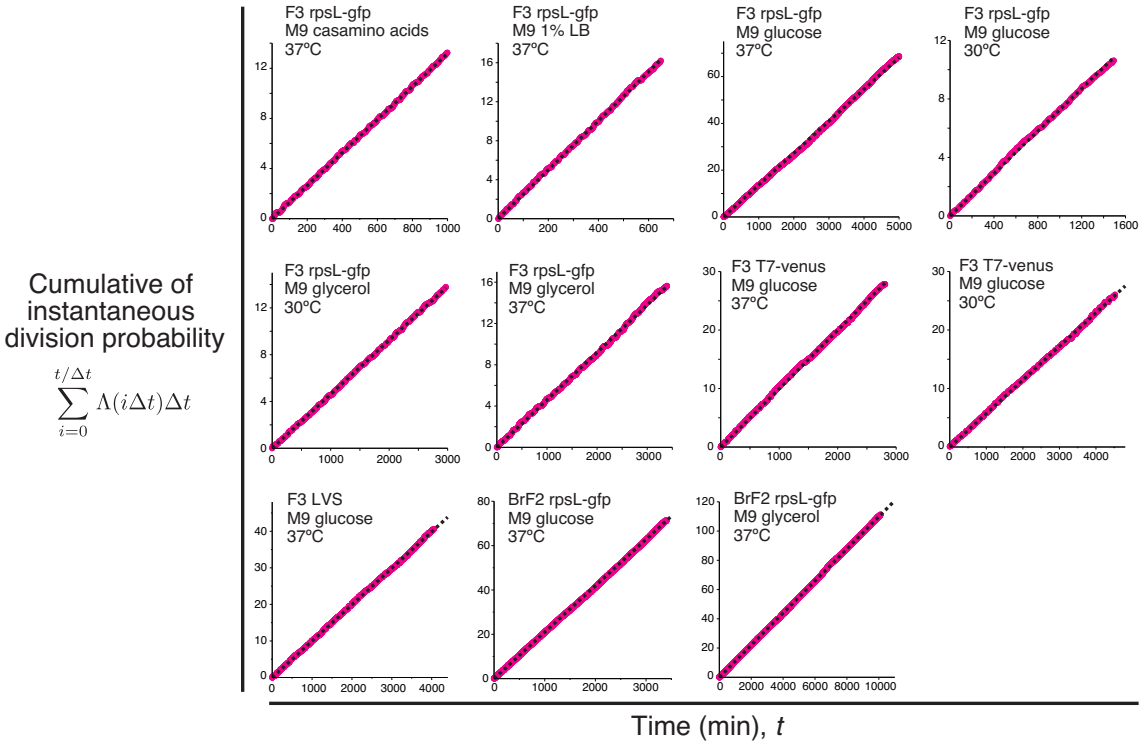

Figure S2: Stability of Growth Rates in Dynamics Cytometer. We defined instantaneous division rate at time t as $\Lambda(t) = \frac{1}{\Delta t} \log\left(1 + \frac{D(t)}{N(t)}\right)$, where Δt is time-lapse interval; $N(t)$ is the number of cells we monitor in the device at t; and $D(t)$ is the number of cells that divided during the time interval $(t, t + \Delta t]$ among $N(t)$ cells. To check the stability of growth rate, we plotted the cumulative of division probability ($\Lambda(t)\Delta t$) against time t ($t/\Delta t$ is the number of time points). The slopes of the plots must be nearly constant if the division rates are stable over the time-course, which is indeed the case here. The broken lines is $y = \Lambda_p t$. The *E. coli* strains and the cultivation conditions are shown on the top-left corner of each plot. The number of division events observed at each time point $D(t)$ is low, which makes the estimate of each value of $\Lambda(t)$ unreliable and requires the introduction of arbitrary time window for averaging. To avoid this, we here plotted the cumulative of division probability instead of directly plotting instantaneous division rate.

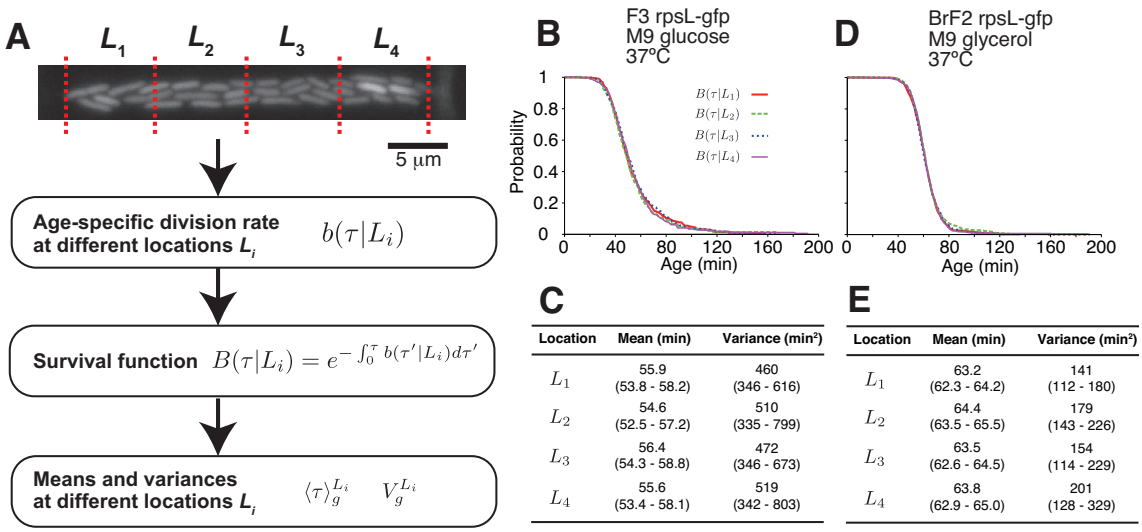

C

Location	Mean (min)	Variance (min²)
L_1	55.9 (53.8 - 58.2)	460 (346 - 616)
L_2	54.6 (52.5 - 57.2)	510 (335 - 799)
L_3	56.4 (54.3 - 58.8)	472 (346 - 673)
L_4	55.6 (53.4 - 58.1)	519 (342 - 803)

E

Location	Mean (min)	Variance (min²)
L_1	63.2 (62.3 - 64.2)	141 (112 - 180)
L_2	64.4 (63.5 - 65.5)	179 (143 - 226)
L_3	63.5 (62.6 - 64.5)	154 (114 - 229)
L_4	63.8 (62.9 - 65.0)	201 (128 - 329)

Figure S3: Location independence of growth statistics within growth channels. A. Outline of the analysis. We first measured age-specific division rate at the different locations $L_1 \sim L_4$ within a growth channel by counting the number of cells with age τ at L_i (represented as $N_a(\tau|L_i)$), and the number of cells that divided between age τ and $\tau + \Delta t$ at L_i (represented as $D_a(\tau|L_i)$). The boundaries of the locations were determined so that the total number of cells $N_{\text{total}}(L_i) = \sum_\tau N_a(\tau|L_i)$ become identical among the different locations L_i. Age-specific division rate $b(\tau|L_i)$ is given by $b(\tau|L_i) = -\frac{1}{\Delta t} \ln\left(\frac{N_a(\tau|L_i) - D_a(\tau|L_i)}{N_a(\tau|L_i)}\right)$. Age-specific division rate $b(\tau|L_i)$ determines $B(\tau|L_i)$, the survival function of generation time distribution by (22), and the mean and variance by (23) and (25), respectively. B-E. Comparison of generation time statistics at different locations in a single growth channel. The results from the experiments for F3 rpsL-gfp in M9 glucose medium at 37°C (B and C) and for BrF2 rpsL-gfp in M9 glycerol medium at 37°C (D and E) are shown. We compared the survival functions (B and D) and the means and variances of generation time (C and E) measured at different locations $L_1 \sim L_4$. The values in the parencies in C and E show the 95% bootstrap confidence intervals.

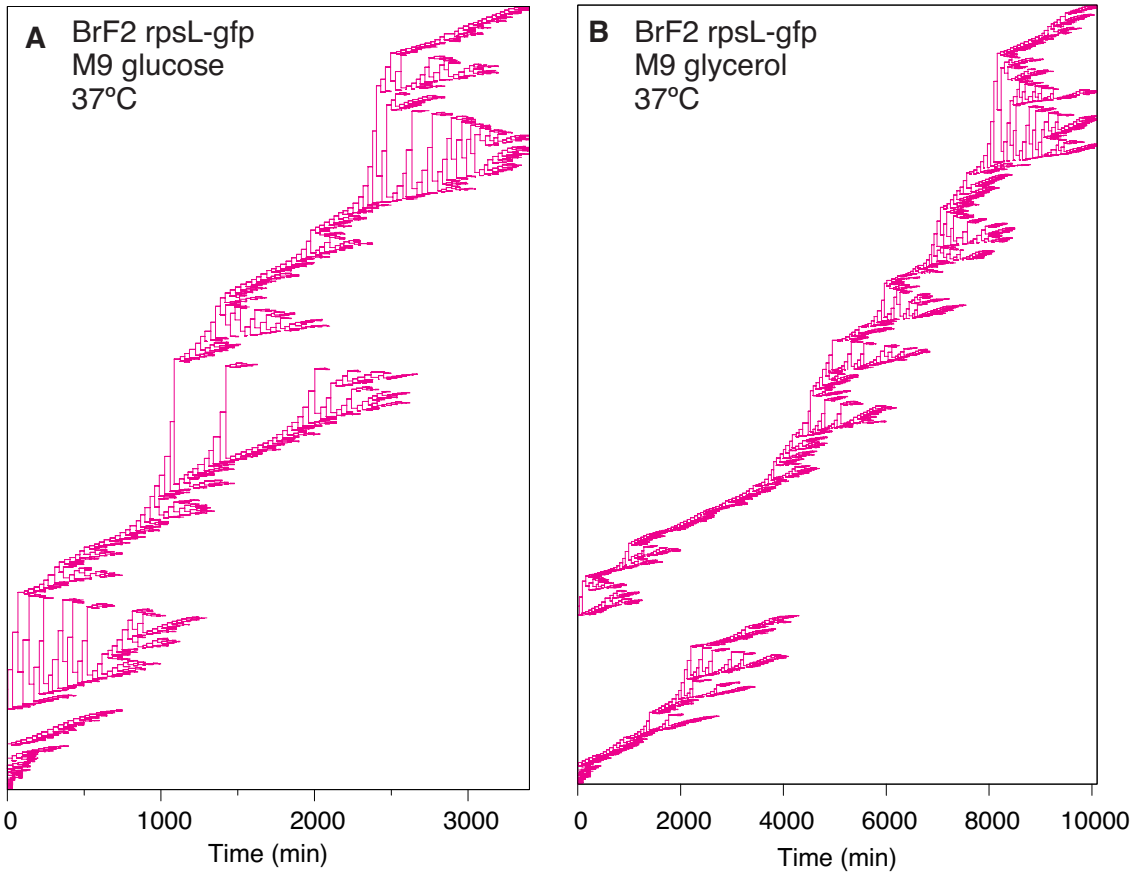

Figure S4: Long Lineage Trees of BrF2. A. Lineage tree of BrF2 in M9 glucose medium at 37°C. B. Lineage tree of BrF2 cultured in M9 glycerol medium at 37°C.

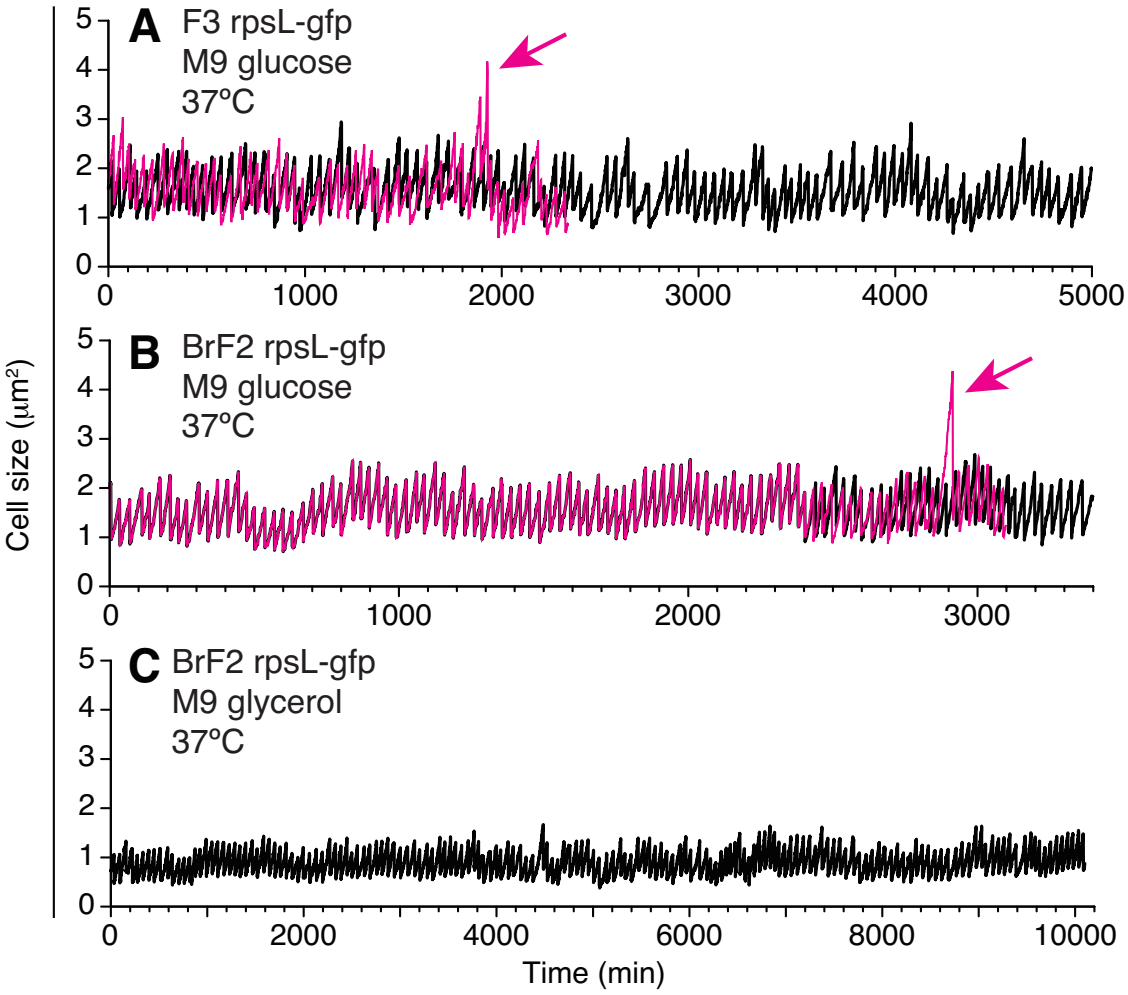

Figure S5: Growth and Division Dynamics along Long Single-Cell Lineages. A. Dynamics of F3 rpsL-gfp strain in M9 glucose medium at 37°C. Black line represents the dynamics of the lineage which stayed in the growth channel over 5,000 min. Magenta line represents the dynamics of a different single-cell lineage, in which a filamentous cell emerged (indicated by the arrow). All the lineages descended from this filamentous cell quickly disappeared from the growth channel. B. Dynamics of BrF2 rpsL-gfp strain in M9 glucose medium at 37°C. In this case, the black and magenta lineages were splitted from the same ancestral cell around $t = 2,400$ min, but the magenta lineage, in which a filamentous cell appeared, again disappeared from the growth channel. C. Dynamics of BrF2 rpsL-gfp strain in M9 glycerol medium at 37°C. In this combination of cell strain and growth condition, we did not observe filamentous cells in any lineages. This is probably due to the fact that the cell size of normal cells in this condition was smaller than that in the other conditions.

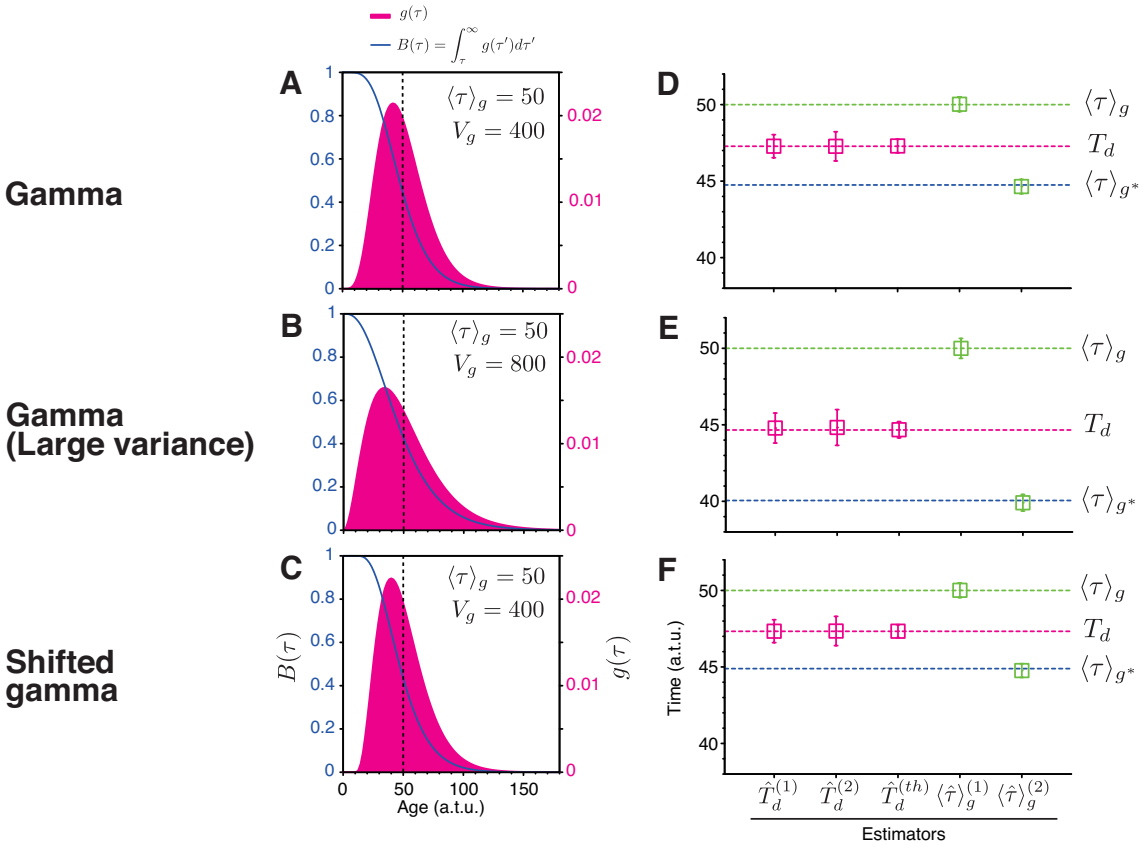

Figure S6: Evaluation of Growth Estimators for Cell Population without Cell Removal. A-C. Generation time distributions used in the simulation: Gamma distribution (A), gamma distribution with large variance (B), and shifted gamma distribution (C). Magenta filled curves show probability density function ($g(\tau)$, on the right axis), and blue curves survival function ($B(\tau) = \int_\tau^\infty g(\tau')d\tau'$, on the left axis). Vertical broken line indicates the common mean of the distributions, $\langle\tau\rangle_g = 50$. D-F. Evaluation of the precision of the estimators under the generation time conditions on the left. Magenta points represent the estimators for population doubling time ($\hat{T}_d^{(1)}$, $\hat{T}_d^{(2)}$, and $\hat{T}_d^{(th)}$, see SI Appendix Text for the definitions), and green points the estimators for mean generation time ($\langle\hat{\tau}\rangle_g^{(1)}$ and $\langle\hat{\tau}\rangle_g^{(2)}$, see SI Appendix Text for the definitions). The error bars are the standard deviations of the estimated values in 1,000 simulation cycles. The horizontal broken lines indicate the true values of the growth parameters: green for $\langle\tau\rangle_g$, magenta for T_d, and blue for $\langle\tau\rangle_{g^*}$.

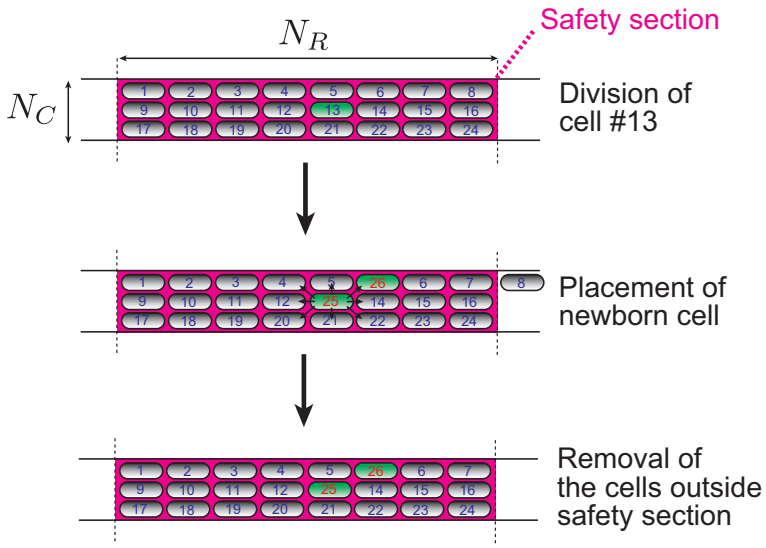

Figure S7: Simulation Cycle of Cell Proliferation in a Condition Similar to Dynamics Cytometer. In this scheme, safety section in the growth channel is shown as the red background, where $(N_R = 8) \times (N_C = 3) = 24$ cells can stay. Each cell division (#13 in this scheme) places two newborn cells, one at the same position (#25), and the other at one of the neighboring positions (#26), and moves a portion of the cells on the same row (#6-#8) toward the right end. If the #26 cell is placed at the position of the #4 cell, the cells #1-#4 will be moved toward the left end. If the #26 cell is placed at the position of the #5 cell, the program randomly chooses the direction of the cell movement: If the right direction is selected, the cells #5-#8 will be moved toward the right end; if the left is selected, the cells #1-#5 will be moved toward the left end. At every check time point with the time interval of 1 a.t.u., the program removes the cells outside the safety section. By repeating this procedure for the duration of 5,000 a.t.u., we exported the datasets of cell proliferation for the analysis.

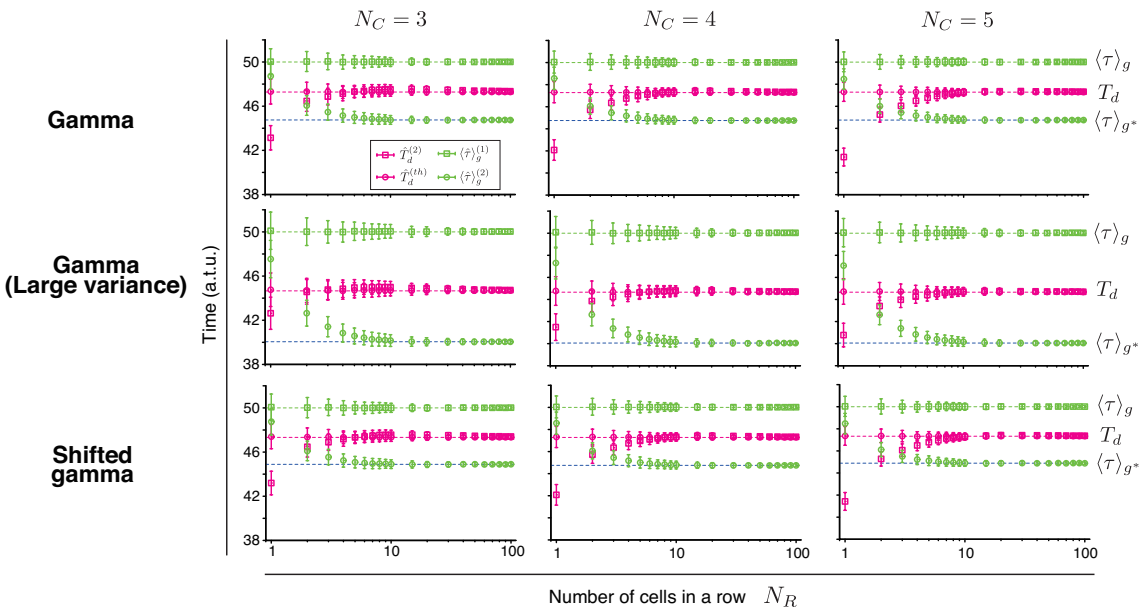

Figure S8: Evaluation of Growth Estimators for Cell Population with Cell Removal. We examined the precision of the estimators using the simulation datasets produced under different conditions of generation time distribution, the number of cells in each column of cell array in the safety section of growth channel (N_C), and the number of cells in each row (N_R). Magenta points represent the population doubling time estimators: Square for $\hat{T}_d^{(2)}$, and circle for $\hat{T}_d^{(th)}$. Green points represent the mean generation time estimators: Square for $\langle\hat{\tau}\rangle_g^{(1)}$, and circle for $\langle\hat{\tau}\rangle_g^{(2)}$. The error bars are the standard deviations of the estimated values in 1,000 simulation cycles. The horizontal broken lines indicate the true values of the growth parameters: green for $\langle\tau\rangle_g$, magenta for T_d, and blue for $\langle\tau\rangle_{g^*}$.

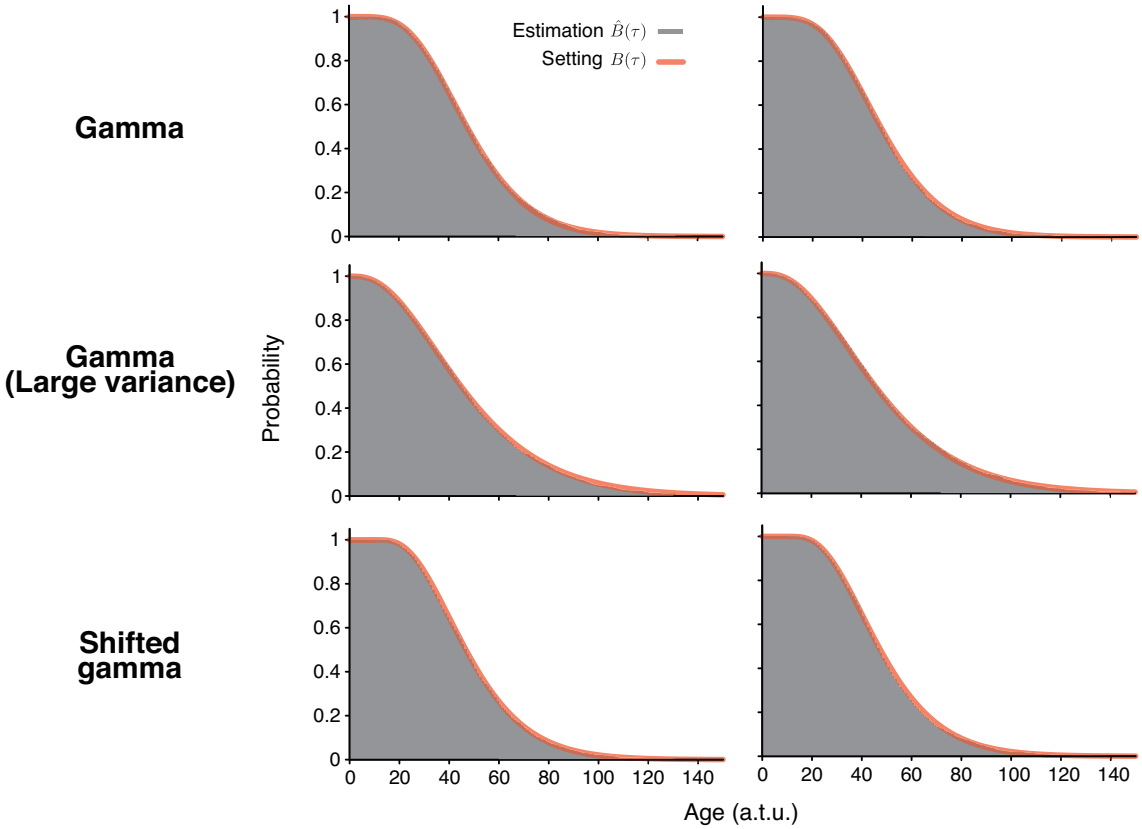

Figure S9: Estimator $\hat{B}(\tau)$ Retrieves the Survival Functions of Pre-Assigned Generation Time Distributions in the Simulation. Gray histograms represent the estimator $\hat{B}(\tau)$. Red curves represents the pre-assigned survival function $B(\tau)$.

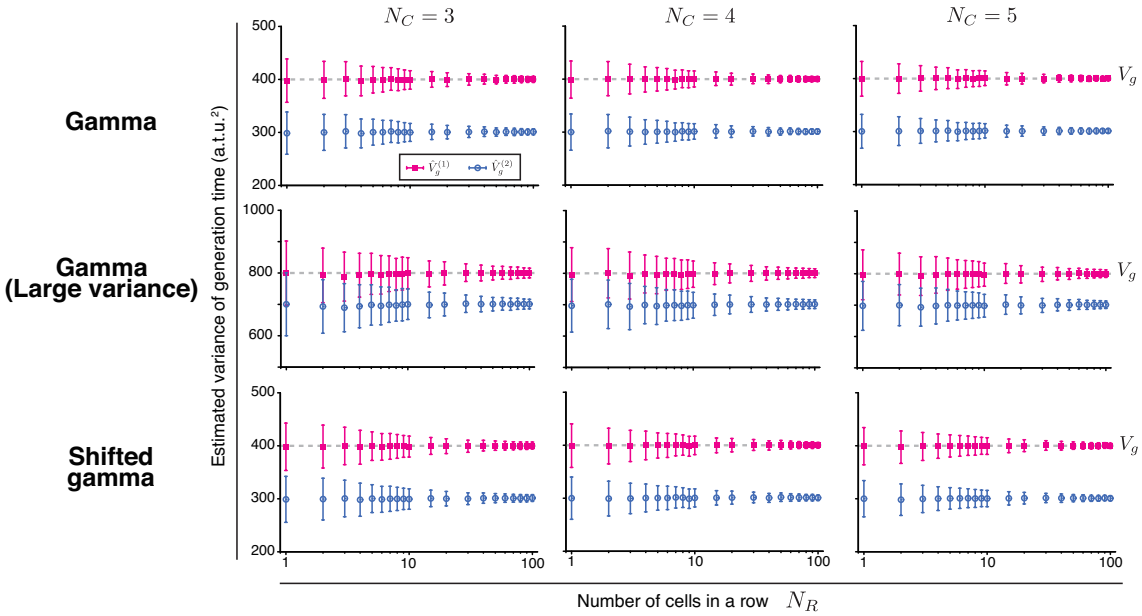

Figure S10: Evaluating the Estimators for the Variance of Generation Time When Applied to the Simulation Datasets with Cell Removal. Magenta squares and blue circles represent the estimator $\hat{V}_g^{(1)}$ and $\hat{V}_g^{(2)}$, respectively (see (25) and (26) for the definitions). The error bars are the standard deviations of the estimated values in 1,000 simulation cycles. $\hat{V}_g^{(1)}$ retrieves the true values of variance (horizontal broken lines).

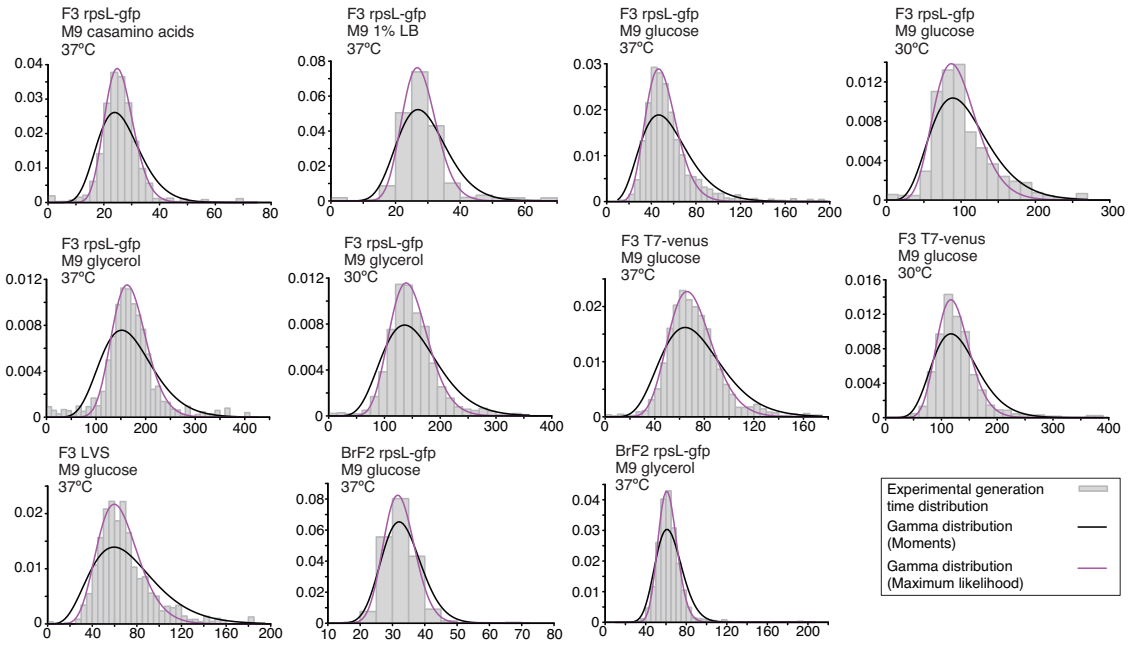

Figure S11: Generation Time Distributions. Gray histograms are experimentally measured $g(\tau)$ according to the estimator (24). The black curves represent the gamma distributions ($\frac{\tau^{k-1}e^{-\tau/\theta}}{\Gamma(k)\theta^k}$, where k is shape parameter, and θ is scale parameter) with their means and variances identical to the experimental distributions (method of moments). The magenta curves represent the gamma distributions estimated by a method of maximum likelihood using the histogram data. The *E. coli* strains and culture conditions are shown at the upper-left corner of each panel.

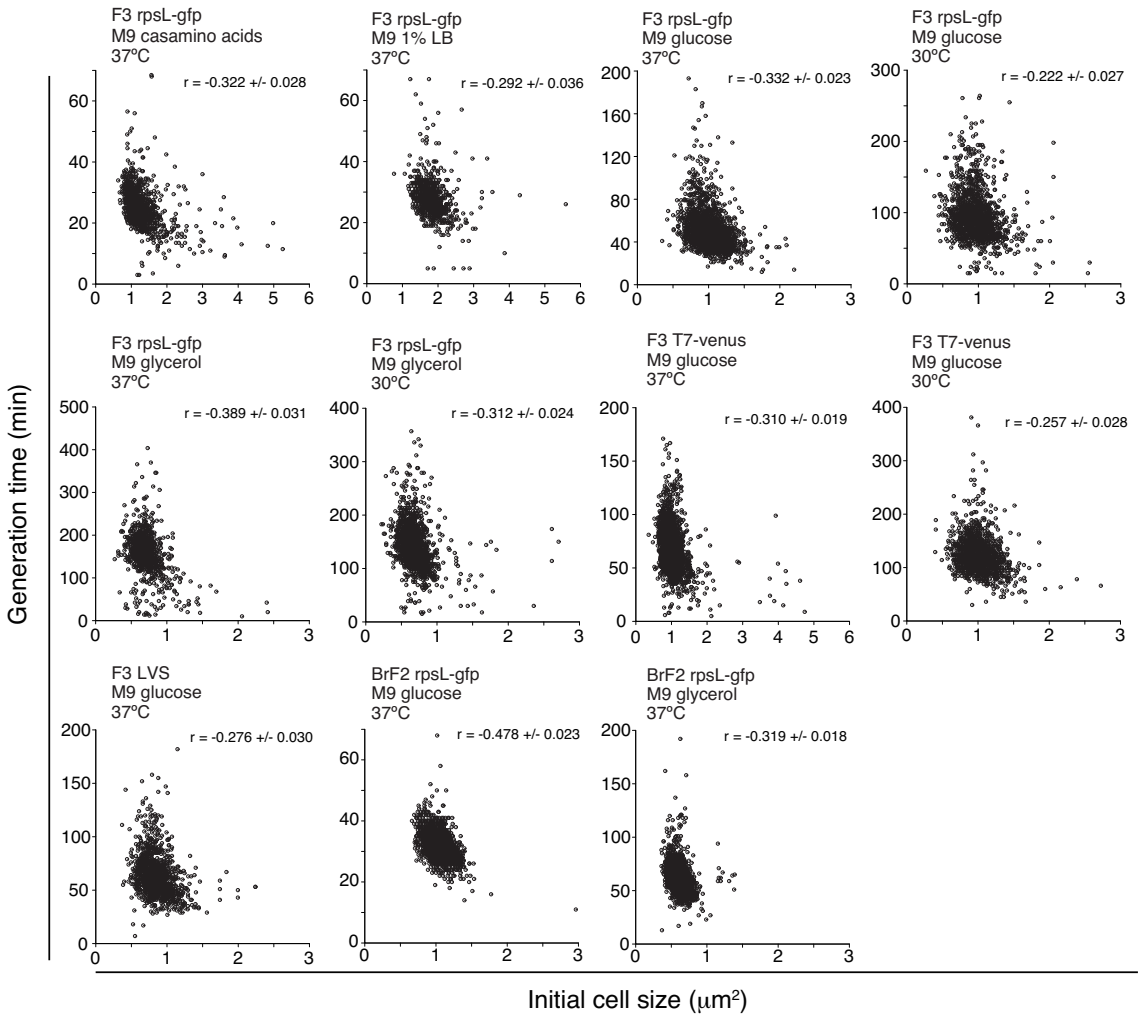

Figure S12: Correlations between Initial Cell Size and Generation Time in Constant Environments. We sampled the data of initial cell size and generation time from the cells which were born and reached the next division in the lineage trees. Pearson correlation coefficients (r) are shown in each panel, which are all slightly negative.